

High-burn-up structure evolution in polycrystalline UO_2: Phase-field modeling investigation

Dan Sun(孙丹), Yanbo Jiang(姜彦博), Chuanbao Tang(唐传宝), Yong Xin(辛勇), Zhipeng Sun(孙志鹏), Wenbo Liu(柳文波), and Yuanming Li(李垣明)

Citation: Chin. Phys. B, 2025, 34 (**2**): 026102. DOI: 10.1088/1674-1056/ad9c42
Journal homepage: http://cpb.iphy.ac.cn; http://iopscience.iop.org/cpb

What follows is a list of articles you may be interested in

Effect of grain size on gas bubble evolution in nuclear fuel: Phase-field investigations

Dan Sun(孙丹), Qingfeng Yang(杨青峰), Jiajun Zhao(赵家珺), Shixin Gao(高士鑫), Yong Xin(辛勇), Yi Zhou(周毅), Chunyu Yin(尹春雨), Ping Chen(陈平), Jijun Zhao(赵纪军), and Yuanyuan Wang(王园园)
Chin. Phys. B, 2024, 33 (**1**): 016105. DOI: 10.1088/1674-1056/ad08a6

Structural evolution and bandgap modulation of layered *β*-$GeSe_2$ single crystal under high pressure

Hengli Xie(谢恒立), Jiaxiang Wang(王家祥), Lingrui Wang(王玲瑞), Yong Yan(闫勇), Juan Guo(郭娟), Qilong Gao(高其龙), Mingju Chao(晁明举), Erjun Liang(梁二军), and Xiao Ren(任霄)
Chin. Phys. B, 2022, 31 (**7**): 076101. DOI: 10.1088/1674-1056/ac6db8

Irradiation-induced void evolution in iron: A phase-field approach with atomistic derived parameters

Yuan-Yuan Wang(王园园), Jian-Hua Ding(丁建华), Wen-Bo Liu(柳文波), Shao-Song Huang(黄绍松), Xiao-Qin Ke(柯小琴), Yun-Zhi Wang(王云志), Chi Zhang(张弛), Ji-Jun Zhao(赵纪军)
Chin. Phys. B, 2017, 26 (**2**): 026102. DOI: 10.1088/1674-1056/26/2/026102

Quantitative determination of anti-structured defects applied to alloys of a wide chemical range

Jing Zhang(张静), Zheng Chen(陈铮), Yongxin Wang(王永欣), Yanli Lu(卢艳丽)
Chin. Phys. B, 2016, 25 (**11**): 116102. DOI: 10.1088/1674-1056/25/11/116102

Phase field modeling of the ring-banded spherulites of crystalline polymers: The role of thermal diffusion

Wang Xiao-Dong (王晓东), Ouyang Jie (欧阳洁), Su Jin (苏进), Zhou Wen (周文)
Chin. Phys. B, 2014, 23 (**12**): 126103. DOI: 10.1088/1674-1056/23/12/126103

High-burn-up structure evolution in polycrystalline UO_2: Phase-field modeling investigation

Dan Sun(孙丹)[1,†], Yanbo Jiang(姜彦博)[2,†], Chuanbao Tang(唐传宝)[1], Yong Xin(辛勇)[1], Zhipeng Sun(孙志鹏)[1], Wenbo Liu(柳文波)[2], and Yuanming Li(李垣明)[1,‡]

[1] *National Key Laboratory of Nuclear Reactor Technology, Nuclear Power Institute of China, Chengdu* 610213, *China*
[2] *School of Nuclear Science and Technology, Xi'an Jiaotong University, Xi'an* 710049, *China*

(Received 26 September 2024; revised manuscript received 10 November 2024; accepted manuscript online 10 December 2024)

Understanding the evolution of microstructures in nuclear fuels under high-burn-up conditions is critical for extending fuel refueling cycles and enhancing nuclear reactor safety. In this study, a phase-field model is proposed to examine the evolution of high-burn-up structures in polycrystalline UO_2. The formation and growth of recrystallized grains were initially investigated. It was demonstrated that recrystallization kinetics adhere to the Kolmogorov–Johnson–Mehl–Avrami (KJMA) equation, and that recrystallization represents a process of free-energy reduction. Subsequently, the microstructural evolution in UO_2 was analyzed as the burn up increased. Gas bubbles acted as additional nucleation sites, thereby augmenting the recrystallization kinetics, whereas the presence of recrystallized grains accelerated bubble growth by increasing the number of grain boundaries. The observed variations in the recrystallization kinetics and porosity with burn-up closely align with experimental findings. Furthermore, the influence of grain size on microstructure evolution was investigated. Larger grain sizes were found to decrease porosity and the occurrence of high-burn-up structures.

Keywords: high-burn-up structure, phase field, uranium dioxide, gas bubble, recrystallization

PACS: 61.80.Az, 62.20.D–, 61.72.Qq

DOI: 10.1088/1674-1056/ad9c42 **CSTR:** 32038.14.CPB.ad9c42

1. Introduction

UO_2 fuel is renowned for its exceptional irradiation stability, extensive operational history within reactors, and robust industrial production infrastructure, rendering it the preferred fuel option for major commercial pressurized water reactors.[1,2] Nonetheless, UO_2 fuel manifests intricate in-reactor dynamics during service owing to fission-induced generation of solid fission products and fission gases, notably Xe and Kr, which undermine fuel efficacy and present safety hazards to nuclear reactors.[2,3] Consequently, the microstructural evolution of fuel under irradiation has been a long-standing focal point of research in the field.

Fission gases tend to aggregate into bubbles owing to their limited solubility in UO_2. At lower burn-up levels, internal bubbles within UO_2 have been documented. However, these internal bubbles tend to saturate as burn up escalates.[4–6] In contrast, intergranular bubbles exhibit larger dimensions.[7] As the average burn up of fuel rods reaches the range of 40–50 GWd/tU and the local burn up at the radial periphery of fuel rods surpasses 60–80 GWd/tU, the inception of high-burn-up structures (HBSs) ensues.[8–10] Concurrently, with the progression of burn up, UO_2 grains undergo a refinement process from their manufactured state to an average size of 0.3 μm.[11] Initially, grain refinement is observed at grain boundaries and newly formed micrometer-sized pores. Beyond a burn up of 108 GWd/tU, the original grain structure is uniformly refined into submicrometer-sized grains, accompanied by the emergence of numerous micrometer-sized pores distributed approximately evenly.[11] Xe migrates into these micrometer-sized pores, precipitating a pronounced increase in UO_2 porosity as burn up escalates.

Researchers have extensively investigated the evolution of high-burn-up structures and its implications on fuel rod performance.[12–15] However, the precise mechanism underlying the formation of HBS remains a subject of ongoing debate. Among the proposed mechanisms, recrystallization and polygonization are the most plausible, as supported by empirical evidence.[16–22] Rest and Hofman hypothesized that the energy stored within dislocation networks serves as the driving force for nucleation of recrystallization.[17] Once the accumulated energy surpasses a critical threshold, grain refinement occurs, which compensates for the energy required to generate grain boundaries without distortion. Subsequently, Rest refined the model to incorporate the influence of fission gas and impurity atoms diffusing into recrystallization nuclei.[23] Nogita *et al.*, on the other hand, proposed a direct correlation between the formation of HBS and the accumulation of irradiation-induced damage, resulting in the development of dislocation networks.[18] These dislocation networks

†These authors contributed equally to this work.
‡Corresponding author. E-mail: lym_npic@126.com

© 2025 Chinese Physical Society and IOP Publishing Ltd. All rights, including for text and data mining, AI training, and similar technologies, are reserved.

eventually evolve into sub grains, leading to the formation of small grains with large-angle grain boundaries as burn up progresses. Matzke and Spino used ion irradiation techniques to investigate grain subdivision or polygonization in UO_2, suggesting that grain subdivision is pivotal in the formation of HBS in high-burn-up UO_2 fuel.[16] Furthermore, Xiao *et al.* expanded on this research, demonstrating that polygonization and recrystallization coexist, and that both play significant roles in the formation of HBS in UO_2.[22]

Semi-empirical models are commonly used to elucidate the behavior of fission gases within HBS. Pizzocri developed a semi-empirical model based on experimental findings to delineate the evolution of grain size with equivalent burn up. By incorporating the observed grain size alterations, a model for the evolution of the gas atom concentration within the lattice was established based on the diffusion theory.[24] Veshchunov *et al.* used mean-field methods to explore the mechanism of pore coarsening in HBS.[25] However, because of the omission of absolute values pertaining to pore growth over time, this model only predicts the correlation between pore density and porosity and lacks the capability to directly forecast changes in pore density and average pore radius over time.

Phase-field methods have emerged as valuable tools for investigating the evolution of HBS. Abdoelatef *et al.* used a quantitative phase-field model to scrutinize the formation and progression of HBS in polycrystalline UO_2.[26] Notably, this model directly simulates the nucleation process of recrystallization, obviating the need for a priori assumptions and using separate algorithms to simulate sub grain formation. Moreover, the model incorporates the influence of the dislocation size and distribution on HBS, along with the effects of gas bubbles on their formation and evolution. The simulation outcomes underscore the pivotal roles played by dislocation size, distribution, and gas bubble number density in governing the kinetics of HBS formation, subsequently shaping the microstructure and affecting its physical properties. The predictions of the model align well with the threshold dislocation density for HBS formation. However, it currently overlooks the impact of grain size and temperature on dislocation accumulation, focusing solely on their effects on HBS kinetics. On a related note, Liang *et al.* explored recrystallization kinetics in U–Mo fuel by integrating the phase-field model with a rate theory model.[27] This investigation systematically examined the effects of fission rate, initial grain size, and grain morphology on recrystallization kinetics, without considering the nucleation processes of sub grains and fission gas bubbles. Similarly, Jiang *et al.* investigated the role of recrystallization in bubble evolution in U–Mo fuel using the phase-field method, highlighting the interaction between bubbles and grain boundaries.[28] The simulation outcomes revealed that recrystallization augmented the number of grain boundaries, thereby expediting bubble nucleation and growth. Grain boundaries have a significant impact on HBS as microstructural features in materials because of their position as preferred nucleation sites for recrystallized grains and bubbles. However, quantitative analysis of the influence of grain size on the evolution of HBS is still lacking.

This paper presents a novel phase-field model that integrates the coupling between grain refinement and bubble evolution. The model encompasses the formation and growth dynamics of recrystallized grains and gas bubbles, along with the interaction between bubble evolution and recrystallization processes. Furthermore, it examines the influence of grain size on the evolution of HBS in polycrystalline UO_2.

2. Phase-field model

2.1. Total free energy

In this section, a mesoscale phase-field model is formulated to address the evolution of radiation-induced Xe bubbles and recrystallized grains. The model integrates the nucleation of subdivided grains. To simulate the progression of Xe bubbles within the recrystallized UO_2, a set of conserved field variables was used in the phase-field model. These variables encompass the vacancy concentration, $c_{\rm v}(\boldsymbol{r},t)$, and gas atom concentration, $c_{\rm g}(\boldsymbol{r},t)$, representing cascade-induced vacancies and Xe gas atoms, respectively. Furthermore, the model distinguishes between the matrix phase and the bubble phase through a non-conserved order parameter η, which transitions continuously from 1 in the bubble phase to 0 in the matrix phase. Additionally, based on Chen's study,[29] a series of non-conserved order parameters $\phi_i^{\rm d}$ are used to characterize the orientation of the deformed matrix grains, whereas $\phi_i^{\rm r}$ is used to denote the recrystallized grains.

The total free energy F of the system is expressed following the form proposed by Cahn–Hilliard[30] as follows:

$$F = N\int_V [f_{\rm bulk} + f_{\rm poly} + f_{\rm grad} + f_{\rm stored}]{\rm d}V, \tag{1}$$

where N is the number of lattice sites per unit volume; $f_{\rm bulk}$ denotes the bulk free-energy density, which characterizes the energy difference between the matrix phase and the bubble phase. The gradient energy density is denoted by $f_{\rm grad}$, whereas $f_{\rm poly}$ represents the polycrystal energy density. Additionally, $f_{\rm stored}$ represents the stored energy density.

The bulk free-energy density is expressed as

$$f_{\rm bulk}(c_{\rm v},c_{\rm g},\eta) = h(\eta)f^{\rm m}(c_{\rm v},c_{\rm g}) + j(\eta)f^{\rm b}(c_{\rm v},c_{\rm g}), \tag{2}$$

where $f^{\rm m}(c_{\rm v},c_{\rm g})$ and $f^{\rm b}(c_{\rm v},c_{\rm g})$ represent the free-energy densities in matrix phase and in bubble phase, respectively. The functions $h(\eta)$ and $j(\eta)$ serve as interpolating functions with the following forms: $h(\eta) = 1-\eta^3(6\eta^2-15\eta+10)$ and $j(\eta) = \eta^3(6\eta^2-15\eta+10)$. These functions facilitate a

smooth transition of the free-energy density between the matrix phase and the bubble phase.

The formulation of the free-energy density in the matrix phase is derived from thermodynamics consisting of the entropic and enthalpy of point defects,[31] and can be expressed as

$$f^{\mathrm{m}}(c_{\mathrm{v}},c_{\mathrm{g}}) = E_{\mathrm{v}}^{\mathrm{f}}c_{\mathrm{v}} + E_{\mathrm{g}}^{\mathrm{f}}c_{\mathrm{g}} + k_{\mathrm{B}}T[c_{\mathrm{v}}\ln(c_{\mathrm{v}}) + c_{\mathrm{g}}\ln(c_{\mathrm{g}}) + (1-c_{\mathrm{v}}-c_{\mathrm{g}})\ln(1-c_{\mathrm{v}}-c_{\mathrm{g}})], \tag{3}$$

where $E_{\mathrm{v}}^{\mathrm{f}}$ and $E_{\mathrm{g}}^{\mathrm{f}}$ are the formation energies of vacancy and gas atom, respectively; k_{B} is Boltzmann's constant, and T is the absolute temperature in Kelvin.

The occupancy of vacancies and gas atoms within the bubble phase is acknowledged. In this study, the configuration of vacancies and gas atoms within a bubble is taken into consideration when formulating the free-energy density within the bubble phase, which is written as

$$f^{\mathrm{b}}(c_{\mathrm{v}},c_{\mathrm{g}}) = c_{\mathrm{g}}k_{\mathrm{B}}T\left(\frac{1}{V-c_{\mathrm{g}}b} - \frac{1}{V}\left(1+\ln\left(n_{\mathrm{Q}}\left(\frac{V}{c_{\mathrm{g}}}-b\right)\right)\right)\right) + A(1-c_{\mathrm{v}})^2, \tag{4}$$

where the first term is the Gibbs free-energy density derived from the van der Waals equation of gas atoms, as a reference in thermal physics.[32] V denotes the volume of the Xe gas atom, n_{Q} is the quantum concentration, and b is the van der Waals constant. The second term embodies a parabolic function associated with vacancies, ensuring the maintenance of $c_{\mathrm{v}} = 1.0$ within the bubble phase, where A represents the pre-factor.[33]

In this study, the progression of deformed and recrystallized grains is accounted for by using a set of order parameters. Consistent with our previous study,[28] the energy density of the polycrystal also encapsulates the interplay between GBs and bubbles, which is expressed as follows:

$$\begin{aligned} &f^{\mathrm{poly}}(\eta,\phi_i^{\mathrm{d}},\phi_i^{\mathrm{r}}) \\ &= \mu\left[\frac{1}{4}\left(\sum_i(\phi_i^{\mathrm{d}})^4 + \sum_i(\phi_i^{\mathrm{r}})^4 + \eta^4\right)\right. \\ &\quad - \frac{1}{2}\left(\sum_i(\phi_i^{\mathrm{d}})^2 + \sum_i(\phi_i^{\mathrm{r}})^2 + \eta^2\right) + \gamma_{\mathrm{r}}\sum_i\sum_{j>i}(\phi_i^{\mathrm{r}})^2(\phi_j^{\mathrm{r}})^2 \\ &\quad + \gamma_{\mathrm{d}}\sum_i\sum_{j>i}(\phi_i^{\mathrm{d}})^2(\phi_j^{\mathrm{d}})^2 + \gamma_{\mathrm{rd}}\sum_i\sum_j(\phi_i^{\mathrm{r}})^2(\phi_j^{\mathrm{d}})^2 \\ &\quad \left.+ \gamma_{\mathrm{b}}\eta^2\left(\sum_i(\phi_i^{\mathrm{d}})^2 + \sum_i(\phi_i^{\mathrm{r}})^2\right)\right], \end{aligned} \tag{5}$$

where μ is the energy coefficient related to the interfacial energy. The parameters γ_{r}, γ_{d}, and γ_{rd} characterize the diffuse interface, each set to a value of 1.5; γ_{b} is the parameter governing the bubble surface and determined by the expression $\gamma_{\mathrm{b}} = \gamma_{\mathrm{r}}E_{\mathrm{surf}}/E_{\mathrm{GB}}$, where E_{surf} denotes the surface energy and E_{GB} represents the GB energy.[27] This formulation of the polycrystal energy guarantees that the free energy at the bubble surface and grain boundaries exceeds that of the grain interior.

The gradient energy term accounts for the free energy arising from the respective interface and can be expressed as

$$f_{\mathrm{grad}}(c_{\mathrm{v}},c_{\mathrm{g}},\eta,\phi) = \frac{\kappa_{cv}}{2}|\nabla c_{\mathrm{v}}|^2 + \frac{\kappa_{cg}}{2}|\nabla c_{\mathrm{g}}|^2 + \frac{\kappa_{\eta}}{2}|\nabla\eta|^2 + \frac{\kappa_{\phi}}{2}|\nabla\phi_i^{\mathrm{r}}|^2 + \frac{\kappa_{\phi}}{2}|\nabla\phi_i^{\mathrm{d}}|^2, \tag{6}$$

where κ_{cv}, κ_{cg}, κ_{η}, and κ_{ϕ} are the gradient coefficients of c_{v}, c_{g}, η, and ϕ, respectively.

The stored energy density attributed to dislocations within the deformed grains, commonly acknowledged as the driving force behind recrystallization, is delineated by the following equation:

$$f_{\mathrm{stored}}(\phi_i^{\mathrm{d}}) = \frac{1}{2}(\phi_i^{\mathrm{d}})^2 G b_{\mathrm{v}}^2\rho, \tag{7}$$

where G represents the shear modulus; b_{v} denotes the magnitude of the Burgers vector; and ρ denotes the mean dislocation density within each deformed grain, which is considered constant for simplification. Based on experimental measurements,[34] the alteration of dislocation density with burn up adheres to the expression $\ln\rho = 2.2\times10^{-2}bu + 13.8$, where bu is the burn up of fuel (in GWd/tU). Furthermore, dislocations were absent in the recrystallized grains.

2.2. Evolution equations

In this study, the modified Cahn–Hilliard equations were formulated to govern the temporal and spatial evolution of conserved field variables encompassing the concentration of vacancies and gas atoms. The formulation is expressed as follows:

$$\frac{\partial c_{\mathrm{v}}}{\partial t} = \nabla\left(M_{\mathrm{v}}\nabla\frac{\delta F}{\delta c_{\mathrm{v}}}\right) + \xi_{\mathrm{v}}(\boldsymbol{r},t) + P_{\mathrm{v}}(\boldsymbol{r},t) - S_{\mathrm{v}}(\boldsymbol{r},t), \tag{8}$$

$$\frac{\partial c_{\mathrm{g}}}{\partial t} = \nabla\left(M_{\mathrm{g}}\nabla\frac{\delta F}{\delta c_{\mathrm{g}}}\right) + \xi_{\mathrm{g}}(\boldsymbol{r},t) + P_{\mathrm{g}}(\boldsymbol{r},t), \tag{9}$$

where M_{v} and M_{g} represent the mobility of vacancies and Xe atoms, respectively, which can be characterized by their corresponding diffusion coefficients, formulated as $M_{\mathrm{v}} = D_{\mathrm{v}}c_{\mathrm{v}}/k_{\mathrm{B}}T$ and $M_{\mathrm{g}} = D_{\mathrm{g}}c_{\mathrm{g}}/k_{\mathrm{B}}T$; ξ_{v} and ξ_{g} denote random terms that represent the thermal fluctuation of point defects. P_{v} and P_{g} denote the source terms that introduce vacancies and gas atoms into the system during irradiation, respectively. S_{v} and S_{g} represent the absorption terms, respectively, depicting the absorption of point defects by dislocations within deformed grains.

The production term of vacancies resulting from a cascade event is expressed as

$$P_{\mathrm{v}}(\boldsymbol{r},t) = \begin{cases} 0 & \text{if } \eta \geq 0.8 \text{ or } R_1 > P, \\ R_2 V_{\mathrm{G}} & \text{if } \eta < 0.8 \text{ and } R_1 \leq P, \end{cases} \tag{10}$$

where P represents the probability of a cascade event occurring at each grid point and time step and is determined by the fission rate. R_1 and R_2 are random numbers ranging between zero and one. V_G denotes the maximum increase in vacancy concentration when a cascade occurs. Additionally, the total vacancy production rate is expressed as $\bar{V}_G = 0.5V_G$, where represents the average increase in vacancy concentration. The production rate K, measured in displacements per atom (DPA) per unit time,[35] can be related to the fission rate through the formulation $f_r = B_f K$, where f_r denotes the fission rate, and B_f is a conversion factor with a value of 2×10^{23} cm^{-3}.[36]

The production term of gas atom is defined as

$$P_g(r,t) = 2(1-\eta)^2 \Lambda \Omega f_r R_3, \tag{11}$$

where Λ is a constant, Ω represents the volume of the UO_2 lattice sites, f_r denotes the fission rate, and R_3 is a stochastic number that ranges between zero and one, as outlined in Ref. [37].

The absorption terms S_v are written as

$$S_v(r,t) = s_v(c_v - c_v^{eq})\Phi, \tag{12}$$

where s_v is a constant that represents the strength of the defects absorbed by GBs. Φ is a formula related to the position and takes the form $\Phi(r,t) = \sum_i (\phi_i^d)^2$, ensuring that any position within the deformed grain interior satisfies $\Phi = 1.0$.

All order parameters are governed by the modified Allen–Cahn equations, which are written as

$$\frac{\partial \eta}{\partial t} = -L\frac{\delta F}{\delta \eta}, \tag{13}$$

$$\frac{\partial \phi_i^d}{\partial t} = -L\frac{\delta F}{\delta \phi_i^d}, \tag{14}$$

$$\frac{\partial \phi_i^r}{\partial t} = -L\frac{\delta F}{\delta \phi_i^r}, \tag{15}$$

where L is the mobility of the free surface. All parameters of UO_2 used in the phase-field simulation are listed in Table 1.

Table 1. Parameters of UO_2 used in the phase-field simulation.

Parameter	Symbol	Value	Reference
Reference length scale (nm)	$l*$	100	this study
Reference timescale (s)	$t*$	1×10^7	this study
Temperature (K)	T	673	this study
Lattice constant (nm)	a	0.547	[39]
van der Waals gas constant (nm^3/atom)	b	0.085	[40]
Shear modulus (GPa)	G	73	[18]
Burgers vector (nm)	b_v	0.39	[18]
Mobility (m^3/(J·s))	L	1.56×10^{-10}	[33]
Surface energy (J/m^2)	E_{surf}	1.80	[41]
GB energy (J/m^2)	E_{GB}	1.04	[42]
Gradient energy coefficient (J/m)	κ	1.60×10^{-7}	[33]
Gas atom formation energy (eV)	E_g^f	8.19	[43]
Vacancy formation energy (eV)	E_v^f	0.59	[44]
Gas atom diffusion coefficient (nm^2/s)	D_g	9.3×10^{-3}	[45]
Vacancy diffusion coefficient (nm^2/s)	D_v	0.96	[33]
Energy coefficient (J/m^3)	μ	6.24×10^7	[46]

Throughout the numerical implementation, the evolution equations are tackled in a non-dimensionalized manner, using nondimensional grid spacing ($x = l/l^*$), time step ($\tau = t/t^*$), and diffusivity ($\tilde{D}_v = D_v t^*/l^{*2}$ and $\tilde{D}_g = D_g t^*/l^{*2}$). This approach uses the reference length scale $l^* = 100$ nm and the timescale $t^* = 1 \times 10^7$ s. The dimensionless evolution equations can be expressed as

$$\frac{\partial c_v}{\partial \tau} = \tilde{\nabla}\left(\tilde{M}_v \tilde{\nabla}\frac{\delta F}{\delta c_v}\right) + \tilde{\xi}_v(\boldsymbol{x},\tau) + \tilde{P}_v(\boldsymbol{x},\tau) - \tilde{S}_v^{GB}(\boldsymbol{x},\tau), \tag{16}$$

$$\frac{\partial c_g}{\partial \tau} = \tilde{\nabla}\left(\tilde{M}_g \tilde{\nabla}\frac{\delta F}{\delta c_g}\right) + \tilde{\xi}_g(\boldsymbol{x},\tau) + \tilde{P}_g(\boldsymbol{x},\tau), \tag{17}$$

$$\frac{\partial \eta}{\partial \tau} = -\tilde{L}\frac{\delta F}{\delta \eta}, \tag{18}$$

$$\frac{\partial \phi_i^d}{\partial \tau} = -\tilde{L}\frac{\delta F}{\delta \phi_i^d}, \tag{19}$$

$$\frac{\partial \phi_i^r}{\partial \tau} = -\tilde{L}\frac{\delta F}{\delta \phi_i^r}, \tag{20}$$

where $\tilde{\nabla} = l^*\nabla$ is the nondimensionalized operator. Additionally, a semi-implicit Fourier spectral method, as introduced in Zhu's work,[38] was used to solve all variable-mobility Cahn–Hilliard equations and Allen–Cahn equations under periodic boundary conditions.

3. Results and discussion

3.1. Recrystallized grain formation and growth

During dynamic recrystallization, the nucleation and growth processes of recrystallized grains must be considered simultaneously. Because the phase-field model cannot directly express the nucleation process, the following nucleation model was used to introduce recrystallized grains. The nucleation model discussed in this section has two important characteristics: the nucleation rate and critical size of the nucleus. The Arrhenius-type nucleation rate model is able to describe the

overall nucleation behavior:[46]

$$\dot{n} = C\dot{\varepsilon}\exp\left(-\frac{Q_{\rm n}}{RT}\right), \tag{21}$$

where C is a constant, $\dot{\varepsilon}$ is the strain rate, and $Q_{\rm n}$ is the activation energy of nucleation. The constant is $C = 6.20\times10^{7}$ m^{-2}, and the stain rate is $\dot{\varepsilon} = 0.002$ s^{-1}.[46] The strain rate was considered a constant in this model. To obtain the activation energy of nucleation, it is necessary to calculate the free-energy change caused by a recrystallized grain. The assumption that the grain is spherical was applied in this model. The refined grains decreased the bulk free energy. However, these grains introduced extra GB areas, which led to an increase in interfacial energy increase. The free-energy change ΔG caused by a single recrystallized nucleus is shown as

$$\Delta G = -\frac{4}{3}\pi r^3\Delta f + 4\pi r^2 E_{\rm GB}, \tag{22}$$

where r is the radius of the nucleus, Δf is the bulk free-energy difference between the deformed and recrystallized grains, and $E_{\rm GB}$ is the GB energy. The first term in Eq. (2) represents the reduction in the bulk free energy, and the second term represents the increase in interfacial energy. It is well known that the stored energy results in a higher free energy in the deformed grains. Thus, the bulk free-energy difference can be expressed as

$$\Delta f = \frac{1}{2}Gb_{\rm v}^2\rho, \tag{23}$$

where G is the shear modulus, $b_{\rm v}$ is the module of Burgers vector, and ρ is the dislocation density. It was assumed that the dislocation density was uniformly distributed in each deformed grain. The free-energy change caused by a single recrystallized grain when ρ takes the saturated value of 5×10^{14} m^{-2} is shown in Fig. 1. The black curve in the figure shows an increase in the surface energy, and the red curve shows a reduction in the bulk free energy. The total free energy is plotted as a blue curve, and there is a maximum value of the total free energy, which is considered the activation energy of nucleation. The grain radius corresponding to the maximum energy is known as the critical radius. In the current simulation, nucleation occurred at GBs, and the nucleation rate per unit area of GB can be obtained using Eq. (22). Therefore, the time step required for one nucleus created is $(\dot{n}\tau n_{\rm gb}x^2/\delta)^{-1}$,[47] where $n_{\rm gb}$ is the grid point number of GBs, and δ is the thickness of GB.

The growth of the recrystallized grains also has an important influence on the recrystallization process. Further, the effect of the dislocation density provided by the deformed grain on the growth of individual recrystallized grains was investigated because the stored energy was recognized as the driving force of refined grain growth. According to the previous calculation, the dislocation density required for a recrystallized grain with a radius of r growth is

$$\rho = \frac{4\gamma_{\rm GB}}{Gb_{\rm v}^2 r}. \tag{24}$$

A single recrystallized grain with a critical radius is placed within the deformed grain matrix. After the same time evolution, the morphology of the single recrystallized grain under different dislocation densities (3×10^{14} m^{-2}, 5×10^{14} m^{-2}, and 7×10^{14} m^{-2}) is plotted in Fig. 2. As shown in Fig. 2, the grain size increased with an increase in the dislocation density. This is because a larger dislocation density leads to a higher free energy in the deformed grain, which is the driving force for the refined grain growth.

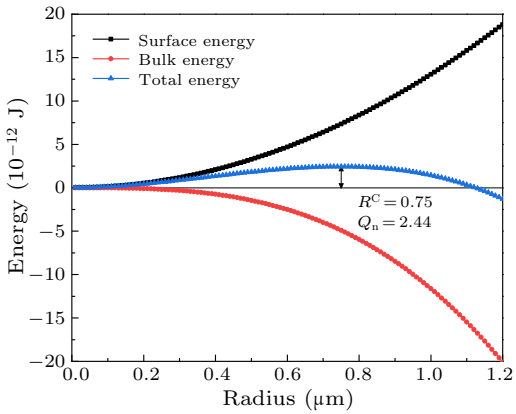


Fig. 1. Free-energy change caused by single recrystallized grain.

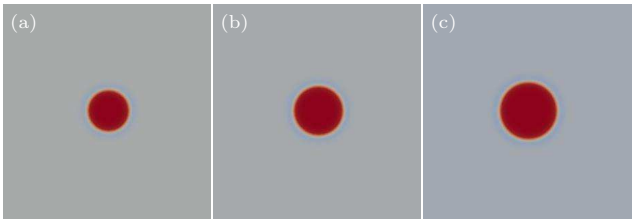


Fig. 2. Morphology of the single recrystallized grain under different dislocation densities: (a) 3×10^{14} m/m^3, (b) 5×10^{14} m/m^3, and (c) 7×10^{14} m/m^3.

To further investigate the effect of the dislocation density, we compared the variation in the grain radius with dimensionless time at different dislocation densities. As shown in Fig. 3(a), the recrystallized grain grows only if the condition meets the critical dislocation density. When the dislocation density is not large enough, the grain shrinks owing to the curvature drive.[48] With an increase in dislocation density, the driving force provided by the stored energy was greater than that of the curvature, resulting in grain growth. In addition, we studied the average growth rate of the recrystallized grain at different dislocation densities. A positive value of the growth rate represents grain growth, whereas a negative value indicates grain shrinkage. As shown in Fig. 3(b), the average growth rate of the recrystallized grain varied linearly with the dislocation density. The grain growth rate was zero at the critical dislocation density. When the dislocation density was greater than the critical value, the grain growth rate

increased with an increase in density. When the dislocation density was smaller than the critical value, the grain shrinkage rate increased with a decrease in density. The current phase-field model is consistent with the theoretical analysis.

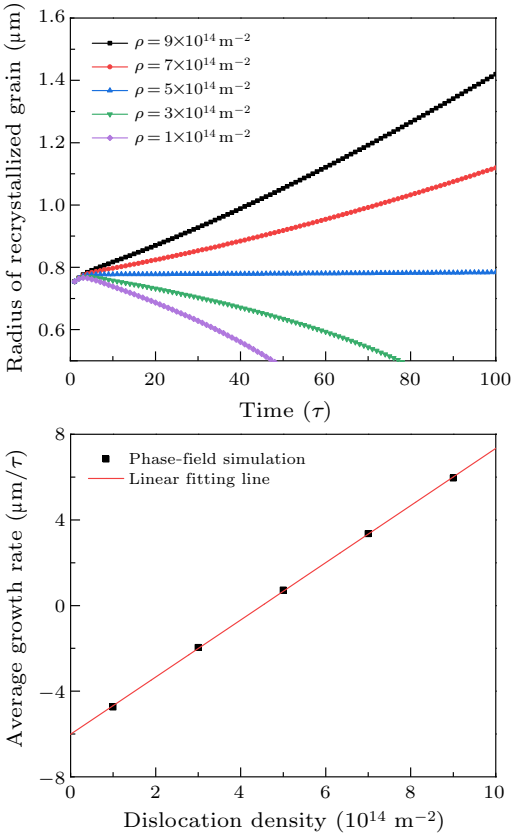


Fig. 3. (a) Variation of grain radius with dimensionless time. (b) The average growth rate of the recrystallized grain.

3.2. Recrystallization in polycrystalline UO_2

We then studied the formation and evolution of recrystallized grains in UO_2 according to the nucleation model built earlier. The simulations were performed in a two-dimensional square domain with $512\Delta x \times 512\Delta y$. As shown in Fig. 4(a), the initial structure consisted of 32 randomly oriented grains with a grain size of approximately 4.53 μm. In addition, for simplicity, all initial grains were assumed to have the same dislocation density. The evolution of recrystallization with burn up is shown in Fig. 4. It can be seen that the recrystallized grains initially formed at the GBs of the deformed grains. The interfaces between the deformed and recrystallized grains became nucleation sites. With the increase in burn up, recrystallized grains gradually developed from the GBs into the grains, and eventually the recrystallization structure filled the whole area. In addition, the nucleation and growth of refined grains occurred simultaneously, which resulted in the recrystallized grains located at the initial GBs with a larger grain size.

The variation in the recrystallization fraction with burn up and the fitted line are plotted in Fig. 5. The evolution of recrystallization follows the nucleation and growth laws. This can be divided into three stages. The first stage is the incubation period, in which the dislocation density and stored energy increase, but the evolution has not yet started, and there is no new grain nucleation. The second stage is the growth stage, during which recrystallized grains begin to nucleate and grow. The third stage is the saturation stage, in which the recrystallization evolution is almost complete, resulting in the inhibition of the nucleation and growth of the refined grains. It is well known that the classical Kolmogorov–Johnson–Mehl–Avrami (KJMA) equation can be used to model a tissue transformation process with nucleation and growth.[49,50] The classical KJMA equation used to describe the recrystallization process can be expressed as[51]

$$X = 1 - \exp(-k(bu)^n). \tag{25}$$

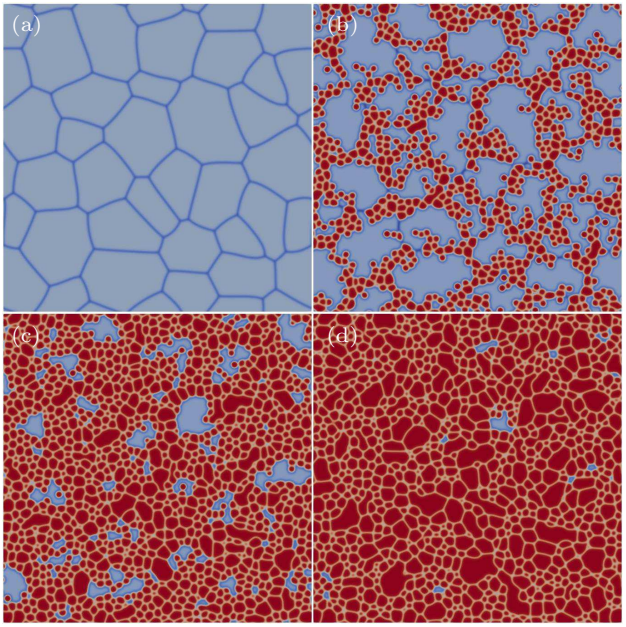


Fig. 4. Recrystallization in polycrystalline UO_2 with the burn up for (a) 0, (b) 72 GWd/tU, (c) 108 GWd/tU, and (d) 140 GWd/tU. The light blue composition in the figure represents deformed grains, the dark blue composition represents the GBs of the deformed grains, the red composition represents the recrystallized grains, and the white composition represents the GBs of the recrystallized grains.

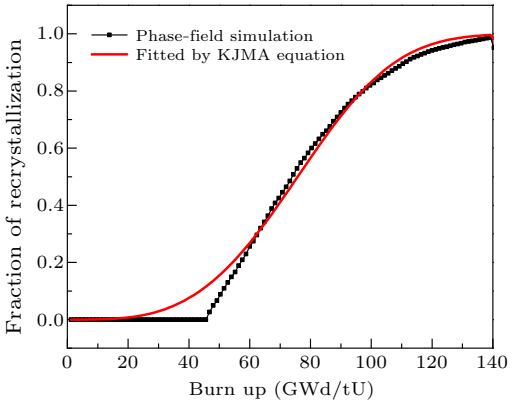


Fig. 5. Variation of the recrystallization fraction with burn up.

Here, X is the fraction of recrystallization, bu is the burn up, k is the kinetic constant, and n is the Avrami constant. As

shown in Fig. 5, the phase-field simulation results are in good agreement with the KJMA equation. The fitting parameters are $k = 2.7 \times 10^{-7}$ and $n = 3.41$.

3.3. Recrystallization coupling bubble evolution

The complex interaction between bubbles and recrystallized grains makes it difficult to study the evolution of high combustion structures. In this section, a phase-field model that considers the evolution of recrystallization and bubble is proposed. The initial structure used in this section is the same as that described in Subsection 3.2. The fission rate and temperature are 1.09×10^{13} fiss/m^3·s and 673 K,[46] respectively. The evolution of the UO_2 microstructure with increasing burn up is shown in Fig. 6. It can be observed that bubbles and recrystallized grains tend to form at the GBs. The experimental and simulation results both show that the existing bubbles and recrystallized grains provide extra nucleation sites for each other, thus enhancing the kinetics of recrystallization and bubble evolution.[52,53] With an increase in burn up, both the number and size of recrystallized grains and bubbles increased. The bubbles and recrystallized grains gradually filled the whole area. Compared to the typical high-burn-up structure morphology observed in the experiment,[52,53] the morphology of the high-burn-up structure in the simulation is in good agreement.

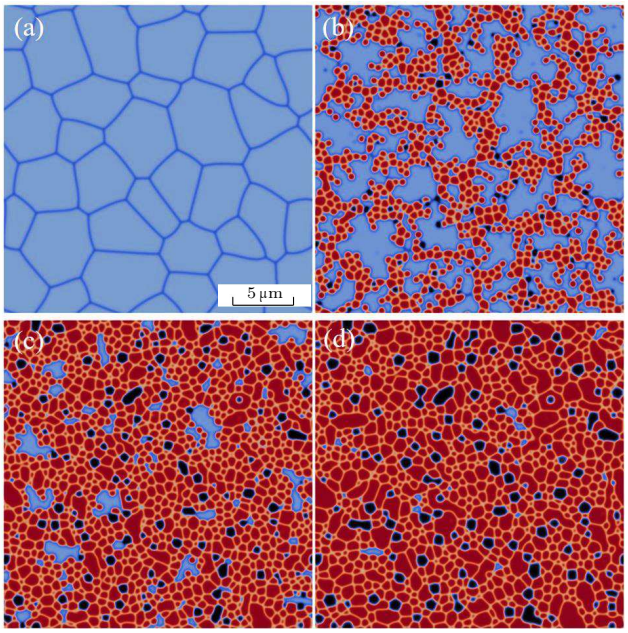


Fig. 6. Recrystallization coupling bubble evolution with the burn up for (a) 0, (b) 72 GWd/tU, (c) 108 GWd/tU, and (d) 140 GWd/tU. The light blue composition in the figure represents deformed grains, the red composition represents the recrystallized grains, and the black composition in the figure is a bubble.

To verify the phase-field model of the HBS evolution, the simulation results were compared with the experimental measurements of Gerczak *et al.*.[52] As shown in Fig. 7, the variation in the recrystallization fraction with burn up conforms to the KJMA equation and is in good agreement with the experimental data. To reveal the effect of gas bubble evolution on the kinetics of recrystallization, the recrystallization fraction of grain refinement coupled with bubble evolution (case 1) was compared to that of grain refinement without bubble evolution (case 2). The Avrami constant fitted according to case 2 is $n = 3.41$, whereas case 1 is $n = 3.45$. This suggests that the bubbles promoted the evolution of recrystallization.

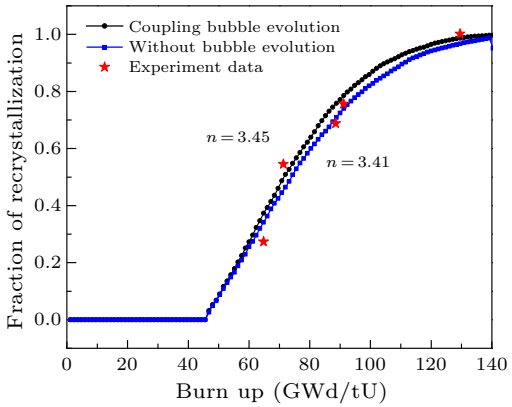


Fig. 7. Variation of the recrystallization fraction with burn up compared with the experimental data.

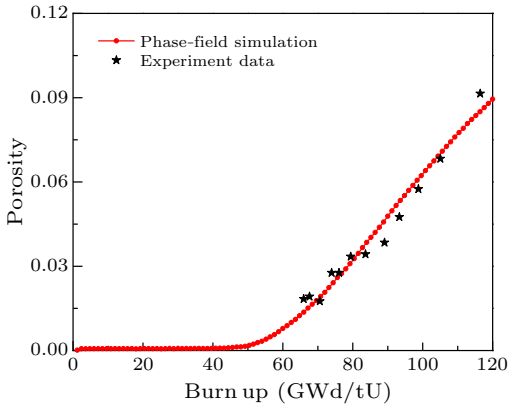


Fig. 8. Variation of the porosity with burn up compared with the experimental data.

During the evolution of the high-burn-up structure, bubbles are continuously formed and grown. Therefore, we also compared the variation in porosity with burn up with the experimental data provided by Gerczak *et al.*[52] As shown in Fig. 8, the simulation results were in good agreement with the experimental results. The figure shows that the evolution of bubbles can be divided into two stages, which is consistent with the conclusion of Millet's study.[31] Stage 1 is the incubation period, in which the concentration of vacancy and gas atom increases, but bubbles do not begin to form until defects accumulate to supersaturation. Stage 2 is the nucleation and growth stage, which occurs after approximately 50 GWd/tU, and the bubble begins to form and grow.

3.4. Effect of grain size

Large-grained UO_2 can suppress fission gas release and intergranular bubble swelling because an enlarged fuel grain

size will extend the length of the diffusion path for fission product gases to grain boundaries.[54] Previous studies have also shown the high resistance of UO_2 to HBS formation at high burn up.[55] To quantitatively analyze the role of grain size on the evolution of high-burn-up structures, several simulations with different initial grain structures were conducted using the verified phase-field model. The microstructures of UO_2 with different grain sizes at 60 GWd/tU are shown in Fig. 9. Except for grain size, the other conditions were completely consistent. It can be seen from the figure that bubbles and recrystallized grains tend to form at GBs. UO_2 with a small initial grain size, has more bubbles and recrystallized grains because of the larger grain boundary area, which provides precipitation sites for bubbles and recrystallized grains. A previous study indicated that grain size affects bubble evolution, with larger grains resulting in a lower porosity rate.[56]

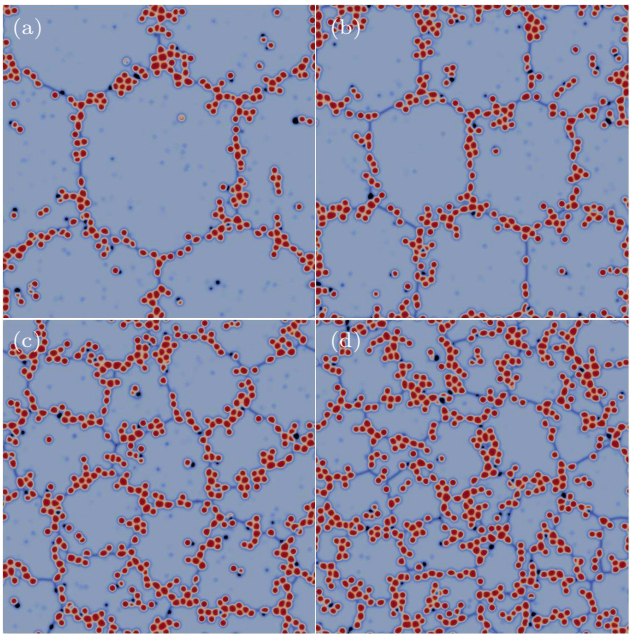


Fig. 9. Morphology of microstructure at 60 GWd/tU with different grain sizes: (a)12.80 μm, (b) 8.53 μm, (c) 6.40 μm, and (d) 4.53 μm.

The recrystallization fraction and porosity of UO_2 with different grain sizes under different burn up are plotted in Fig. 10. The burn up required for the formation of recrystallized grains and gas bubbles in UO_2 with different grain sizes was the same. Furthermore, UO_2, with a smaller grain size, exhibited a rapid increase in both the recrystallization rate and porosity with increasing burn up. By fitting the obtained kinetic curves of the recrystallization fraction under different grain sizes according to the KJMA equation, the variation in the Avrami constant n with grain size is plotted in Fig. 11. The dynamic constant k is fixed as 2.7×10^{-7}. The Avrami constant is almost linearly related to the grain size, as shown in the figure. Therefore, a small grain size promotes the evolution of a high burnup structure. The deduction predicted from the present simulation is in good agreement with the experimental measurements.[18,57,58]

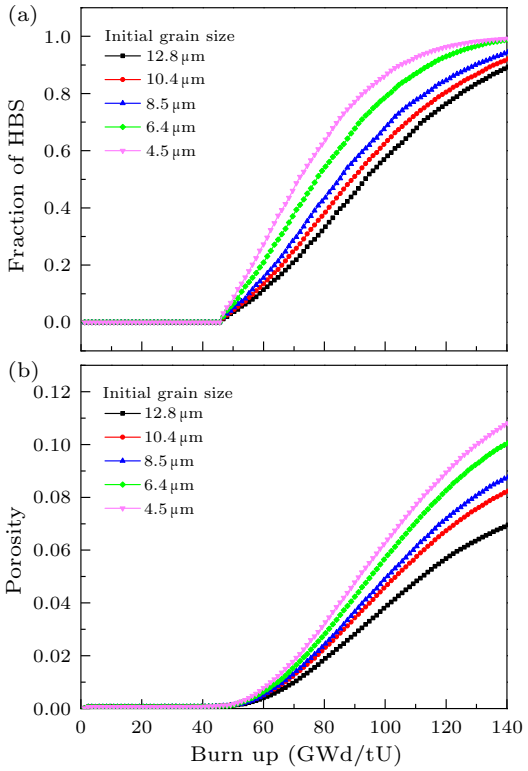


Fig. 10. Variation with burn up under different grain sizes: (a) fraction of HBS and (b) porosity.

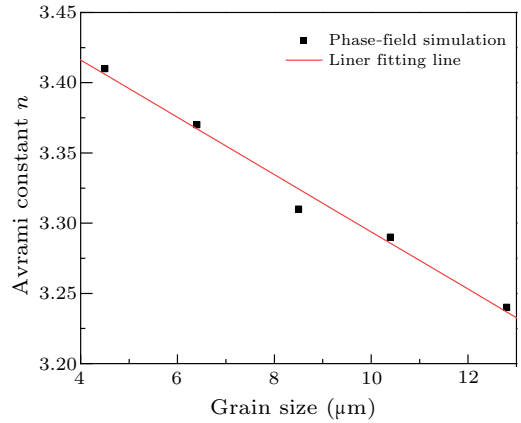


Fig. 11. Variation of Avrami constant n with grain size.

4. Conclusions

In summary, we developed a phase-field model to simulate the evolution of the high-burn-up structure in UO_2. The nucleation and growth of recrystallized grains and bubbles were simultaneously simulated. We also discussed in detail the impact of grain size on recrystallization kinetics and porosity. The main findings are summarized as follows.

(i) Refined grains grow only if they meet the conditions of the critical radius and dislocation density simultaneously. A larger dislocation density provides a greater driving force

for refined grain growth, and the variation in growth rate with dislocation density is approximately linear.

(ii) The kinetics of recrystallization in polycrystalline UO_2 is divided into three stages, which conform to the KJMA equation. As burn up increases, recrystallized grains first form at the grain boundaries and then gradually fill the whole region.

(iii) The morphology of the high-burn-up structure in the simulation was in good agreement with the experimental results. It has been demonstrated that gas bubbles and recrystallized grains mutually promote their evolution. In addition, a smaller grain size enhances the kinetics of recrystallization and gas bubble because of the larger GB area and shorter diffusion distance.

This article provides basic insights into the influence of grain size on HBS, but owing to the limited amount of experimental data, there is still much room for improvement in the model. In the future, the phase-field model can be further optimized by introducing more microscopic mechanisms to enhance its accuracy and applicability. This will help more accurately study the microstructural evolution of uranium dioxide in complex irradiation environments.

Acknowledgements

This study was supported by the National Natural Science Foundation of China (Grant Nos. U20B2013 and 12205286) and the National Key Research and Development Program of China (Grant No. 2022YFB1902401).

References

[1] Ho M, Obbard E and Burr P A 2019 *Energy Procedia* **160** 459
[2] Zinkle S J and Was G S 2013 *Acta. Mater.* **61** 735
[3] Rest J, Cooper M, Spino J, Turnbull J, Van Uffelen P and Walker C 2019 *J. Nucl. Mater.* **513** 310
[4] Cornell R M 1971 *J. Nucl. Mater.* **38** 319
[5] Une K, Kashibe S and Takagi A 2006 *J. Nucl. Sci. Technol.* **43** 1161
[6] Turnbull J A 1971 *J. Nucl. Mater.* **38** 203
[7] Kashibe S and Une K 1991 *J. Nucl. Mater.* **28** 1090
[8] Rondinella V V and Wiss T 2010 *Mater. Today* **13** 24
[9] Matzke H 1992 *J. Nucl. Mater.* **189** 141
[10] Ray I, Thiele H A and Kinoshita M 1997 *J. Nucl. Mater.* **245** 115
[11] Spino J, Stalios A D, Santa H and Baron D 2006 *J. Nucl. Mater.* **354** 66
[12] Matzke H J and Kinoshit M 1997 *J. Nucl. Mater.* **247** 108
[13] Marchetti M, Laux D, Fongaro L, Wiss T, Van Uffelen P, Despaux G and Rondinella V V 2017 *J. Nucl. Mater* **494** 322
[14] Terrani K A, Balooch M, Burns J R and Smith Q B 2018 *J. Nucl. Mater.* **508** 33
[15] Baron D, Kinoshita M, Thevenin P and Largenton R 2008 *Nucl. Eng. Technol.* **41** 199
[16] Matze H and Spino J 1997 *J. Nucl. Mater.* **248** 170
[17] Rest J and Hofman G L 2000 *J. Nucl. Mater.* **277** 231
[18] Nogita K and Une K 1995 *J. Nucl. Mater.* **226** 302
[19] Lee C B and Jung Y H 2000 *J. Nucl. Mater.* **279** 207
[20] Gerezak T J, Parish C M, Edmondson P D, Baldwon C A and Terrani K A 2018 *J. Nucl. Mater.* **509** 245
[21] Miao Y B, Yao T K, Lian J, Zhu S, Bhattacharya S, Oaks A, Yacout A M and Mo K 2018 *Scripta Mater.* **155** 169
[22] Xiao H X, Long C S and Chen H S 2021 *J. Nucl. Mater.* **556** 153151
[23] Rest J 2004 *J. Nucl. Mater.* **326** 175
[24] Pizzocri D, Cappia F, Luzzi L, Pastore G, Rondinella V V and Van Uffelen P 2017 *J. Nucl. Mater.* **487** 23
[25] Veshchunov M S and Tarasov V I 2017 *J. Nucl. Mater.* **488** 191
[26] Abdoelatef M G, Badry F, Schwen D, Permann C, Zhang Y and Ahmed K 2019 *JOM* **71** 4817
[27] Liang L Y, Mei Z G, Kim Y S, Ye B, Hofman G, Anitescu M and Yacout A M 2016 *Comput. Mater. Sci.* **124** 228
[28] Jiang Y B, Xin Y, Liu W B, Sun Z P, Chen P, Sun D, Zhou M Y, Liu X and Yun D 2022 *Nucl. Eng. Technol.* **54** 226
[29] Chen L Q and Yang W 1994 *Phys. Rev. B* **50** 15752
[30] Cahn J W and Hilliard J E 1958 *J. Chem. Phys.* **28** 258
[31] Millett P C, El-Azab A and Wolf D 2011 *Comput. Mater. Sci.* **50** 960
[32] Kittel C and Kroemer H 1980 *Thermal Physics* (New York)
[33] Aageen L K, Biswas S, Jiang W, Andersson D, Cooper M W D and Matthews C 2021 *J. Nucl. Mater.* **557** 153267
[34] Nogita K and Une K 1994 *Nucl. Instrum. Meth. B* **91** 301
[35] Millett P C, El-Azab A, Rokkam S, Tonks M and Wolf D 2011 *Comp. Mater. Sci.* **50** 949
[36] Rest J and Hofman G L 1994 ANL/ET/PP-84776 Argonne National Lab
[37] Liang L Y, Mei Z G, Kim Y S, Anitescu M and Yacout A M 2018 *Comp. Mater. Sci.* **145** 86
[38] Zhu J Z, Chen L Q, Shen J and Tikare V 1999 *Phys. Rev. E* **60** 3564
[39] Schoenes J 1978 *J. Appl. Phys.* **49** 1463
[40] Veshchunov M S 2000 *J. Nucl. Mater.* **277** 67
[41] Matzke H J, Inoue T and Warren R 1980 *J. Nucl. Mater.* **91** 205
[42] Nerikar P V, Rudman K, Desai T G, Byler D, Unal C, McClellan K J, Phillpot S R, Sinnott S B, Peralta P, Uberuaga B P and Stanek C R 2011 *J. Am. Ceram. Soc.* **94** 1893
[43] Andersson D A, Uberuaga B P, Nerikar P V, Unal C and Stanek C R 2011 *Phys. Rev. B* **84** 054105
[44] Matthews C, Perriot R and Cooper M W D 2019 *J. Nucl. Mater.* **527** 151787
[45] Turnbull J A, Friskney C A, Findlay I R, Johnson F A and Walter A J 1982 *J. Nucl. Mater.* **107** 168
[46] Jiang, Y B, La Y X, Liu X X and Liu W B 2024 *J. Nucl. Mater.* **601** 155312
[47] Takaki T, Hirouchi T, Hisakuni Y, Yamanaka A and Tomita Y 2008 *Mater. Trans.* **49** 2559
[48] Vedantam S and Mallick A 2009 *Acta Mater.* **58** 272
[49] Avrami M 1939 *J. Chem. Phys.* **7** 1103
[50] Avrami M 1940 *J. Chem. Phys.* **8** 212
[51] Barani T, Pizzocri D, Cappia F, Luzzi L, Pastore G and Van Uffelen P 2020 *J. Nucl. Mater.* **539** 152296
[52] Gerczak T J, Parish C M, Edmondson P D, Baldwin C A and Terrani K A 2018 *J. Nucl. Mater.* **509** 245
[53] Hiernaut J P, Wiss T, Colle J Y, Thiele H, Walker C T, Goll W and Konings R J M 2008 *J. Nucl. Mater.* **377** 313
[54] Massih A 2014 Swedish Radiation Safety Authority, Uppsala Sweden
[55] Noirot J, Pontillon Y, Yagnik S and Turnbull J A 2015 *J. Nucl. Mater.* **462** 77
[56] Sun D, Yang Q, Zhao J, Gao S, Xin Y, Zhou Y, Yin C, Chen P, Zhao J and Wang Y 2024 *Chin. Phys. B* **33** 016105
[57] Xiao H X, Long C S and Chen H S 2016 *J. Nucl. Mater.* **471** 74
[58] Une K, Nogita K, Kashibe S and Imamura M 1992 *J. Nucl. Mater.* **188** 65